Solute micro-segregation profile and associated precipitation in cast Al-Mg-Si alloy

Artenis Bendo, Jonathan Fellowes, Matthew Smith, Masoud Moshtaghi, Zelong Jin, Kenji Matsuda, Zhongyun Fan & Xiaorong Zhou

View supplementary material

Published online: 05 May 2024.

Submit your article to this journal

Article views: 342

View related articles

View Crossmark data

Solute micro-segregation profile and associated precipitation in cast Al-Mg-Si alloy

Artenis Bendo[a], Jonathan Fellowes[b], Matthew Smith[a], Masoud Moshtaghi[c], Zelong Jin[a], Kenji Matsuda[d], Zhongyun Fan[e] and Xiaorong Zhou[a]

[a]Department of Materials, The University of Manchester, Manchester, UK; [b]Department of Earth and Environmental Sciences, The University of Manchester, Manchester, UK; [c]Laboratory of Steel Structures, LUT University, Lappeenranta, Finland; [d]Graduate School of Science and Engineering, University of Toyama, Toyama, Japan; [e]Brunel Centre for Advanced Solidification Technology, Brunel University London, Uxbridge, UK

ABSTRACT

The micro-segregation in the as-cast AA6082 aluminium alloy were investigated across a range of length scales using a combination of analytical electron microscopes. It is found that the micro-segregation bands form an inter-connected network following grain boundaries and inter-dendritic channels. The micro-segregation can be divided into major micro-segregation and minor micro-segregation; the former is mainly on the grain boundaries consisting of iron-bearing intermetallic; the latter occurs both, along the grain boundaries and inter-dendritic channels, consisting mainly of Mg and Si alloying elements. The atomic-scale imaging reveals that in the minor-segregation bands, the supersaturated solute concertation has formed precipitates that had either nucleated heterogeneously on the dislocation network or homogeneously inside the aluminium matrix. The heterogeneously nucleated precipitates in the dislocation lines are composed of a mixture of phases down the precipitation sequence meanwhile, the homogenously grown ones are discrete phases that appear at the early stages of the precipitation sequence.

Introduction

The solute segregation is a common phenomenon during the solidification of aluminium alloys. It occurs due to non-equilibrium conditions caused by the fast-cooling rates [1]. The advancing front of the solid/liquid interface will create a continuous solute build-up in the melt [2]. Partition coefficient of elements determines whether they will enrich in the solid or liquid phase

during solidification. For solute elements such as Si, Mg, Cu, Zn, Fe and so on, the partition coefficient is less than 1, which means that the solute elements will enrich in liquid phase while the solid phase will become depleted [1]. For Ti and Cr, the partition coefficient is more than 1, which means they will enrich in the solid phase and deplete the liquid one [1].

Depending on the length-scale over which it occurs, segregation can be macro if the distribution occurs at the billet size length-scale and micro if it occurs at μm length-scale [3,4]. Previous reports on macro-segregation in the cast Al-Mg-Si alloys suggest a depletion of Mg and Si at the centre and enrichment near the surface areas of the billet [5]. This is known as negative centreline segregation, and it is caused because Mg and Si have partition coefficient less than 1 [5]. It is reported that the centreline segregations depend on the cooling rate, grain refining additions, chemical composition and so on [1,2,5,6].

In addition to macro-segregation, the micro-segregation also occurs at the level of α-Al dendrites and α-Al grains. The established argument on micro-segregation is that the coarse-dendrites are solute-depleted, meanwhile the fine-cell dendrites are solute-rich or close to the overall composition of the cast [1]. Studies show that the segregation of alloying elements such as Mg and Si increases towards the dendritic arm boundaries and grain boundaries, in accordance with their partition coefficient [7–9].

Previous work suggested the presence of metastable β′ and stable β phases, in addition to the Fe-rich intermetallic within the micro-segregated regions in Al-Mg-Si alloys [6–8,10,11]. However, questions about the concentration gradient and atomic-scale structure of the micro-segregation bands remain unanswered. The Al-Mg-Si alloys are increasingly used for manufacturing of vehicle parts [12]. The AA6082 aluminium alloy achieves one of the best mechanical performances if carried out through the conventional down-stream thermomechanical treatment [13]. However, the industry encourages employment of the parts directly produced in their as-cast conditions, due to cut-down of manufacturing costs related to the down-stream thermomechanical processes. The precipitation of the strengthening phases in wrought Al-Mg-Si alloys requires Mg and Si solute elements, which concentrations are significantly influenced by the micro-segregation profiles. Thus, a thorough understanding of the structure of segregation bands becomes important.

This work provides proofs upon which the micro-segregation is divided into the major and minor. The focus of this work is on the microstructure of the minor micro-segregation bands. The distribution patterns, concentration gradients, and the nano-structures of the minor micro-segregation bands and their relation to the major micro-segregation bands is clarified in this work. To note is that the minor and major micro-segregation is a relative terminology used intentionally for this work to clearly describe the variations within the micro-segregation bands. Therefore, the terms should be considered inside the framework provided here. The elemental maps at micro and sub-micro

length scales are obtained from the as-cast AA6082 aluminium alloy samples produced via three different casting processes. The atomically resolved imaging is used to characterise the fine details of atomic structures of phases present within the minor micro-segregated bands.

Experimental

The cast AA6082 aluminium alloys were prepared at Brunel Centre for Advanced Solidification Technology (BCAST) using conventional direct chill casting (DC), direct chill casting with the addition of Ti and B as grain refiners (DCGR) [14–16] and direct chill casting with melt conditioning (DCMC). The DCMC cast is prepared using the high shear melt conditioning (HSMC), otherwise named intensive shear melting or melt conditioning by advanced shearing technology (MCAST) which are reported elsewhere [17–21].

For the DC and DCGR, the cast was carried out in a mould with diameter of 153 mm and a 150 mm/min withdrawal speed of the shell from the bottom of the mould. The water flow for cooling was 3 L/sec. For melt conditioning by the advanced intensive shear melting technology (MCAST), the speed of the twin-screw rotor was 2000 rotation per minute (rpm). The samples for investigation were cut at the half-altitude bottom to top and half-radius in the as-cast billets.

The overall chemical compositions of the samples were determined using a Thermo Scientific ARL iSpark optical spark emission spectroscopy (SES) and results are shown in the Table 1. The acquisition electronics and treatment algorithms are integrated into the instrument and are controlled by the software. The tests were done according to the ASTM E415 standard.

The samples for scanning electron microscopy (SEM) were prepared using the standard procedure of mechanical polishing with silicon carbide (SiC) paper, then with colloidal silica (OPS) and at the end with polishing cloth. The backscattered electron imaging (BSE) and energy dispersive X-ray spectroscopy (EDS) were carried out in three scanning electron microscopes (SEM), a FEI Quanta 250 field emission gun (FEG), a FEI Quanta 650 FEG and a Tescan Mirai3LC FEG, all operated at 15 kV acceleration, aperture size 50 μm and spot size 6.

The electron probe micro-analysis (EPMA) was carried out in a JEOL JXA-8530F, equipped with Field Emission Gun (FEG), four SP detectors, low range soft X-Ray emission spectrometer (SXES) and EDS. The operation was carried out at 10 kV acceleration voltage, 10 and 100 nA emission current, 50 ms dwelling time and step size of 0.16, 0.2 and 0.5 micron/pixel. The detection limit depending on the sample preparation quality and elements for analysis, can go down to around 10 parts per million (ppm).

For transmission electron microscopy (TEM) investigation, disks were punched out from ~70 μm thick foils and electropolished in a twin-jet polishing machine using a mixed solution of 1/3 nitric acid (HNO_3) and 2/3 methanol (CH_3OH) kept at a temperature range between −20°C and −30°C. The twinjet

Table 1. The compositions (wt. %) and standard deviation (SD) of the as-cast AA6082 Al alloy prepared via direct chill (DC), direct chill casting using melt conditioning (DCMC) and direct chill casting with grain refinement addition Al-5Ti-1B (DCGR).

		Al	Si	Mg	Mn	Fe	Cu	Cr	Ti	V	B	Hf	Ni, Ga, Zn, Ca, Pb, Sr, V, Hg, Y
DC	wt. %	97.3	1.02	0.752	0.489	0.197	0.067	0.063	0.012	0.01	–	0.016	0.024
	SD	0.015	0.003	0.007	0.001	0.002	–	–	–	–	–	0.02	0.001
DCMC	wt. %	97.3	1.08	0.689	0.474	0.187	0.07	0.077	0.027	0.01	–	0.013	0.013
	SD	0.019	0.017	0.003	0.001	0.001	–	–	0.001	–	–	0.001	0.001
DCGR	wt. %	97.4	1.02	0.684	0.478	0.181	0.074	0.067	0.036	0.01	0.002	0.018	0.015
	SD	0.018	0.003	0.007	0.003	0.006	–	–	0.001	–	–	0.001	0.02

electropolished TEM disks were surface cleaned and further thinned using Gatan Precision Ion Polishing System II (PIPS II) with beam energy 4–0.5 kV and an incident angle of ±3°.

Three transmission electron microscopes (TEM) were employed, a FEI Tecnai TF30 Field Emission Gun (FEG) operated at 300 kV, a FEI Talos F200 X-Field Emission Gun (X-FEG) scanning transmission electron microscopes (STEM) operated at 200 kV which was equipped with four Super-X energy dispersive X-ray spectroscopy (EDS) detectors optimised for maximising the EDS signal gathering and a FEI Titan G2 80–200 aberration-corrected scanning transmission electron microscope (STEM) operated at 200 kV with a probe current of 1 nA, a semi-convergence angle of 25 mrad and an inner collection angle of 54 mrad, considered optimal for atomic-scale resolution high angle annular dark field scanning transmission electron microscopy (HAADF-STEM) imaging.

Results and discussion

The samples obtained from the region of interest, which is at half-altitude bottom to top and half-radius in the as-cast billets, are analysed via spark emission spectroscopy (SES). All samples contain two main solute elements, Si and Mg, which serve for the precipitation process and Fe and Mn elements responsible for Fe-rich intermetallic formation (Table 1). The B element is only detected in the grain refined (DCGR) cast. Moreover, the Ti is in highest concentration in the DCGR cast. The excess Ti in DCGR cast is required for forming Al_3Ti layer which wraps the TiB_2 particle [15]. The Al_3Ti layer is considered more effective for heterogeneous nucleation of Al grain than TiB_2 alone, due to better coherency with the Al matrix [15,16].

Major micro-segregation

The major segregation is associated with the formation of coarse features which can be readily observed using SEM. Figure 1 shows the back-scattered
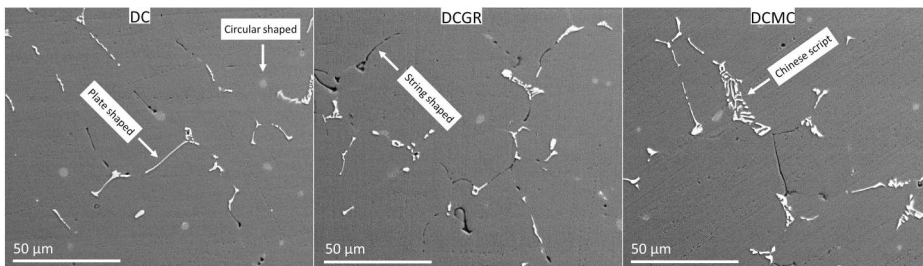
Figure 1. The back-scattered electron SEM images of the microstructure of AA6082 Al alloy in the as-cast DC, DCGR and DCMC conditions. The precipitation of the plate, Chinese script, string and circular shaped features has taken place.

electron images of three casting conditions. The coarse features (tens of μm) are classified based on their morphology, image contrast and composition. Three distinct features are observed. The white-contrast intermetallics of plate and Chinese-script shapes are distributed mainly along the Al grain boundaries, intruding often into the Al grain interiors. The grey-contrast circular-shaped features seem to be distributed independently inside the Al grains and the black-contrast features of string-shaped morphologies are distributed along the Al grain boundaries and often in contact with white-contrast features.

The elemental maps of all observed features are shown in the Figure 2. The white contrast features of plate and Chinese-script morphologies contain mainly Si, Fe and Mn. The Fe and Mn elemental maps overlap almost perfectly. The Mn was present in every phase regardless of their shapes, be it platelet or Chinese script. The circular-shaped ones indicated in the DC condition of Figure 2 are strongly enriched in Si and Mg. Meanwhile, the dark-contrast features are significantly enriched in O, and less in Si and Mg. The pinpoint compositional analysis is carried out in each feature. The results are shown in the Figure 1 in the Appendix.
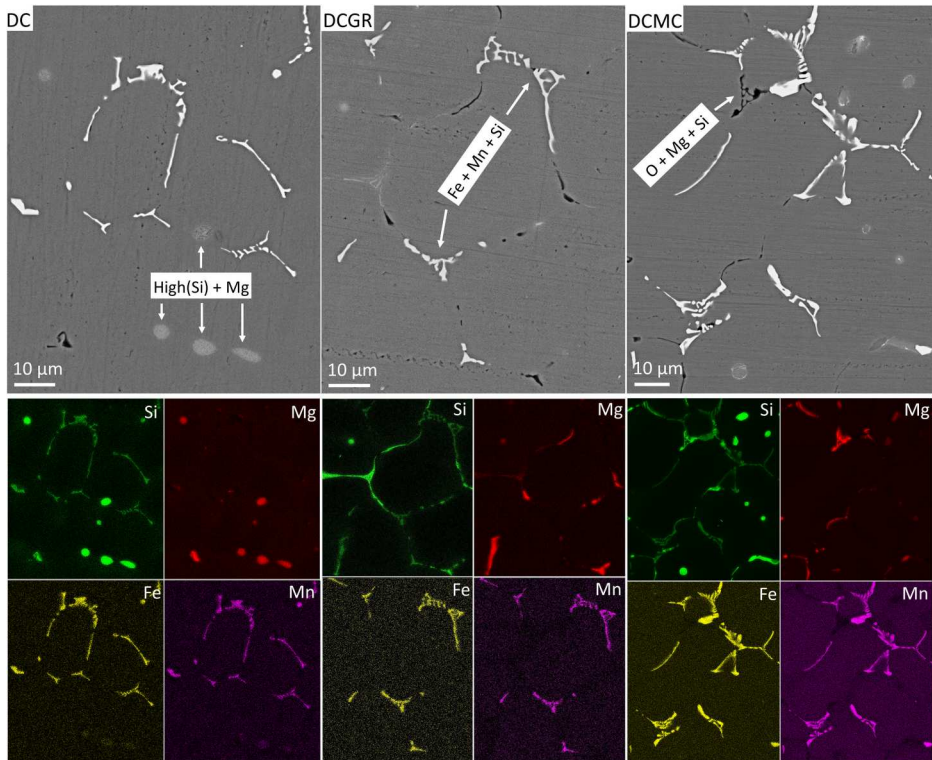
Figure 2. The back-scattered electron images of three casting conditions and the corresponding elemental maps. The labellings show the main element composition of the indicated phases.

Based on the morphology, contrast in the electron backscattered images, elemental mappings and pinpoint compositional analysis, the microstructure in the micrometer scale is mainly formed from the alpha-phase iron-rich inter-metallic, which are the white-contrast of plate-shaped and Chinese-script morphologies, the Si-rich phase which are the circular-shaped grey-contrast features and the Al oxide particles which are the black-contrast features. The alpha-phase and Al oxide particles are mainly distributed along the grain boundaries, in contact to each-other, meanwhile, the Si-rich phases are independently found trapped inside the Al grains.

The solidification during casting normally occurs under non-equilibrium conditions. Having not enough time for solute diffusion, segregation of Fe and other solute elements occurs between the Al dendrites and eventually between the Al grains, at the end of solidification [22]. The solute-enriched areas with the presence of Fe, form intermetallic compounds rich in Fe (Fe-IMCs) [23]. Two main iron-rich intermetallic are the alpha-phase $Al_{15}(FeMn)_3Si_2$ and beta-phase Al_5FeSi, reported as having cross-sections of Chinese-script and needle morphologies, respectively [24]. The alpha-phase has been reported with many different morphologies such as petal, comb and dendritic-like [25]. Serial sectioning of samples and three-dimensional reconstruction based on the arbitrarily selected range of grey-scale intensity of SEM images can be used to discriminate different phases [26]. Serial sectioning revealed that alpha and beta phases are dendritic and plate-like shaped in three-dimensions [27]. Furthermore, the dendritic-arms of the alpha-phase are indeed diverging from a blocky polyhedral morphology [26–28]. The same morphology was also confirmed using phase mapping via electron backscattered diffraction [29].

The thermodynamic calculations for the alloy composition investigated in this work are carried out using Scheil solidification and the results are shown in the Figure 2 in the Appendix. The Scheil solidification assumes no diffusion in the solid and infinite diffusion in the liquid which is akin to fast cooling rate conditions [4]. It predicts that the Al grains nucleate as primary phase, followed by the nucleation of the alpha-phase. The Fe has limited solubility in Al, and it will segregate at the solid–liquid interface of the solidification front of the dendritic Al arms, which will result in the formation of the alpha-phase via a eutectic reaction: enriched solute liquid → Al + α-$Al_{15}(FeMn)_3Si_2$. It will either grow separately or in an intercoupled way with the moving Al solidification front. When the solidified fraction increases beyond approximately 90%, the formation of the beta-phase will take place. The formation of the beta-phase will be favoured because of the lack of Mn which had been already used in the formation of the alpha-phases. Upon complete solidification, the precipitation of the Mg_2Si and Si will take place. The thermodynamic calculation fits well with the SEM experimental results which show that most iron-rich intermetallic are of alpha-phase.

The cooling rate is one important controlling factor for solidification. The increase of the cooling rate promotes formation of the alpha-phase at the expense of the beta-phase and drives the formation of the primary Al by shrinking the time for the formation of the iron-rich intermetallic [25,30]. The primary nucleated Al dendrite will reject and push forward the solute atoms along the solid–liquid interface solidification front, which will give rise to the solute segregation between Al dendrite and Al grain boundaries [31,32]. It indicates that the cooling rate in the investigated region in this work was fast enough to suppress the formation of the beta-phase.

Another important factor is the presence of oxide particles which are observed in all three casting conditions. The oxide particles do not dissolve in the melt and serve as nucleation centre, changing the nucleation sequence described in the thermodynamic calculation. This is important in the DCMC melt, since it is reported that there is a high presence of the individual oxide particles distributed homogeneously in the melt, due to break-down of the oxide film on top of the melt, from the high-shear twin-screw rotor-stator melt-conditioning mechanism [21,33–36]. The main oxides being the MgO, Al_2O_3 and the $MgAl_2O_4$ are observed to serve as nucleation centres for the primary iron-rich intermetallic or primary Al. It is suggested that they also can contribute via multistep nucleation mechanism, such as oxide particle to primary iron-rich intermetallic to aluminium or oxide particle to Al_3Ti to Al [29,36–41].

Minor micro-segregation

The scanning electron microscopy shows the presence of the coarse features such as the iron-bearing intermetallic (Fe-IMCs), Si-rich phases and Al oxide particles. The electron probe micro-analysis (EPMA) is employed to reveal the subtle composition variations which are not possible using SEM-EDS. The EPMA provides the advantage of elemental probing down to ppm levels. Figure 3 shows the EPMA maps of Si and Mg which are contrast enhanced to reveal the fine patterns of segregation. There is a high intensity of segregation along the grain boundaries and a medium to low intensity of segregation which follows the inter-dendritic areas, present in all casting conditions.

The segregation pattern is observed particularly clear in the DCGR cast, inside which almost one entire Al grain is mapped. The segregation pattern reveals the dendritic structure. The primary and secondary Al dendritic arms are revealed due to segregation along the inter-dendritic channels. The grain boundaries show high intensity of segregation with Si and Mg. The intense segregation along the grain boundary diverges towards the grain interior guided by inter-dendritic channels. The intensity of segregation in the divergent inter-dendritic channels is minor compared to the major one along the grain boundaries.
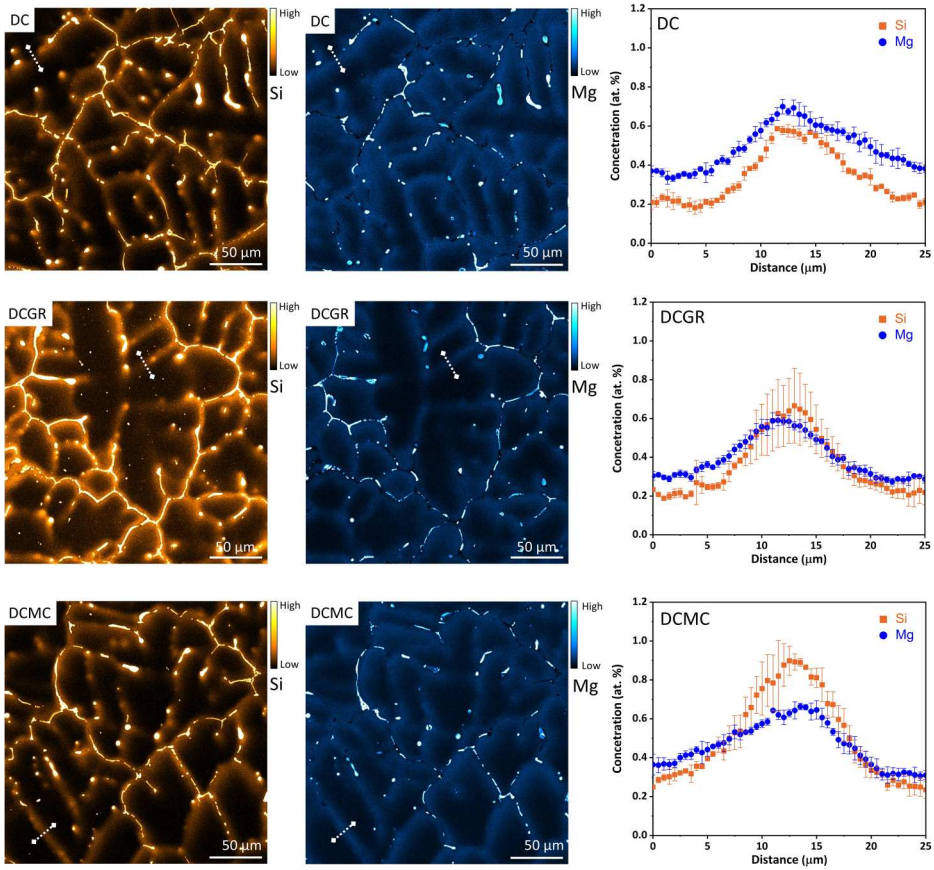
Figure 3. The qualitative electron probe micro-analysis (EPMA) maps of Si and Mg segregation in three different casting conditions. The EPMA maps are purposefully enhanced to reveal the minor segregation bands. The line scans are indicated with white dashed lines. The concentration (at.%) vs distance (µm) plots correspond to the respective line scans in the EPMA maps.

The line-profile scans indicated with white dashed lines are carried out across the minor micro-segregation bands for all three casting conditions. The plots of concentration versus distance, show that the minor-segregation bands are approximately 5–15 µm wide. The Mg and Si enrichment peak at approximately 0.6–0.8 at.%. The minor-segregation bands show variations in concentration of Mg and Si elements.

The minor-segregation bands connect the high-concentration domains located discretely. In other words, the high-concentration local areas of Si and Mg, which correspond to coarse intermetallic alpha-phases, beta-phases and Si-rich phases, are connected from the network of segregation bands of Mg and Si. The Si is present in all phases excluding Al oxides and therefore its segregation map can be used to trace simultaneously the Fe-bearing intermetallic and the precipitates. The Fe-bearing alpha-phase intermetallic are

distributed along the grain boundaries as seen clearly on the Fe segregation map in the DCGR cast in the Figure 3 in the Appendix.

The EPMA elemental maps provide the sensitivity advantage which the EDS lacks. The EDS elemental maps in the Figure 2 can reveal only the high concentration areas where the coarse intermetallic and oxides are located but it is not able to resolve the minor segregated bands. The phases which seem to be independently distributed inside the Al grains (Figure 2), are indeed embedded within a network of minor micro-segregated bands which follow the inter-dendritic channels and grain boundaries as seen in the EPMA maps in Figure 3.

To investigate the fine microstructural details occurring in the minor-segregated bands, scanning transmission electron microscopy (STEM) and transmission electron microscopy (TEM) were employed. The TEM imaging revealed the presence of fine alpha-phases in the minor-segregated bands, an example of which is seen in Figure 4. The Figure 4 shows a hexagonal plate-shaped intermetallic with face length of around 500 nm. The electron diffraction has a 6-fold symmetry, where the main g-vectors bound the hexagon faces of the intermetallic as shown by the white dashed arrows. The elemental maps clearly show that the hexagonal-shaped intermetallic is rich in Si, Fe and Mn. The obtained atomic formula from EDS analysis is $Al_{15.7}$-$(FeMn)_{4.5}Si_{2.7}$. The atomic-scale resolution shows that the high-intensity atomic columns which are rich in Fe or its substitution Mn, match well with the projection along the $\langle 111 \rangle$ direction of the crystal structure proposed by Cooper [42]. To highlight is that the differences between the three proposed crystal structures from Cooper stem from the outer atomic layers which are rich in Al or its substitution Si. This was not possible to be resolved in this case. Considering that the difference in atomic number between Fe and its substitution Mn is negligible, but it is significantly bigger compared to Al or its substituion Si, this is used as a keylock to match the crystal structure with the obtained atomic-resolution image.

The hexagonal-shaped particles of similar size are reported on several occasions. The hexagonal plate-shaped morphology with a 6-fold electron diffraction was classified as β-Mg_2Si stable phase being observed along their $\langle 111 \rangle$ direction [43]. The composition of the hexagonal-shaped particle in those cases was Mg, Si and Cu and length of the hexagonal faces was of round 2–3 μm [43]. It is reported that the β-Mg_2Si crystals could obtain also many different shapes such as octahedron, faceted octahedron, cubes, hopper and dendrite in sizes of tens of μm [44]. On the other hand, polygons of near hexagonal-shaped intermetallic of tens of μm are classified as alpha-phase iron-rich intermetallics [45]. There are two commonly reported crystal structures for the alpha-phase, the cubic α-$Al_{15}(FeMn)_3Si_2$/$Al_{19}(FeMn)_5Si_2$ and the hexagonal α_{hex}-Al_8FeSi [46,47]. The hexagonal alpha-phase is stable without the presence of Mn, meanwhile the cubic alpha-phase requires the presence of Mn [48,49].
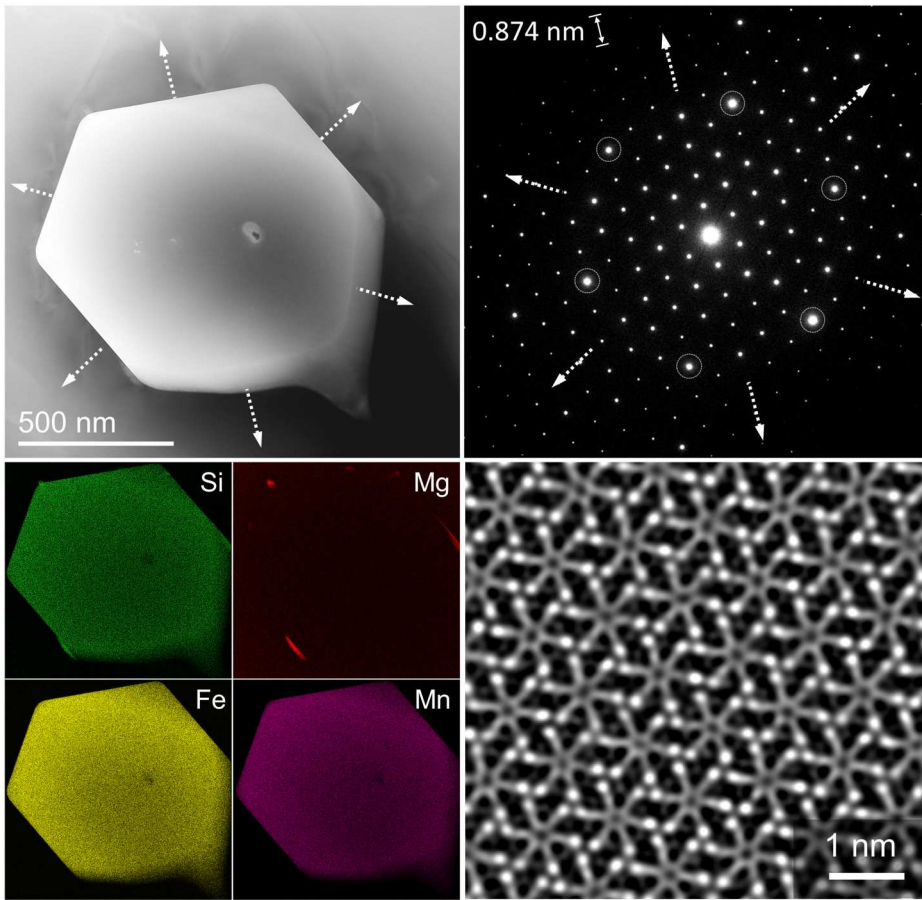
Figure 4. The observed morphology in the micro-segregation bands in the DCGR cast. The TEM image of a hexagonal-shaped alpha-phase iron-rich particle, corresponding electron diffraction, elemental maps and noise filtered atomic-scale HAADF-STEM image along the ⟨111⟩ zone axis of the cubic alpha iron-rich phase.

The Mn promotes the transformation from plate-shaped beta-phase to spheroidic-shaped alpha-phase during homogenisation heat treatment [50–52]. The suppression of the beta-phase is reported to be done by Mn addition or in the absence of Mn, by use of high cooling rates resulting in the formation of the hexagonal alpha-phase [48,50,51,53]. The results of the current work show that the hexagonal-shaped intermetallic in Figure 4 is classified as the cubic alpha-phase iron-rich intermetallic based on the atomic resolution imaging matching and element analysis.

The HAADF-STEM imaging was employed to characterise the minor-segregation band down to atomic-scale level. Figure 5 (A0) shows the STEM image of the microstructure along the $[001]_{Al}$ zone axis, next to a dendrite in the DCGR cast. The nature of the dendrite in the Figure 5 (A0) is not confirmed. Figure 5 (A1) shows that the dislocation lines are entangled in an
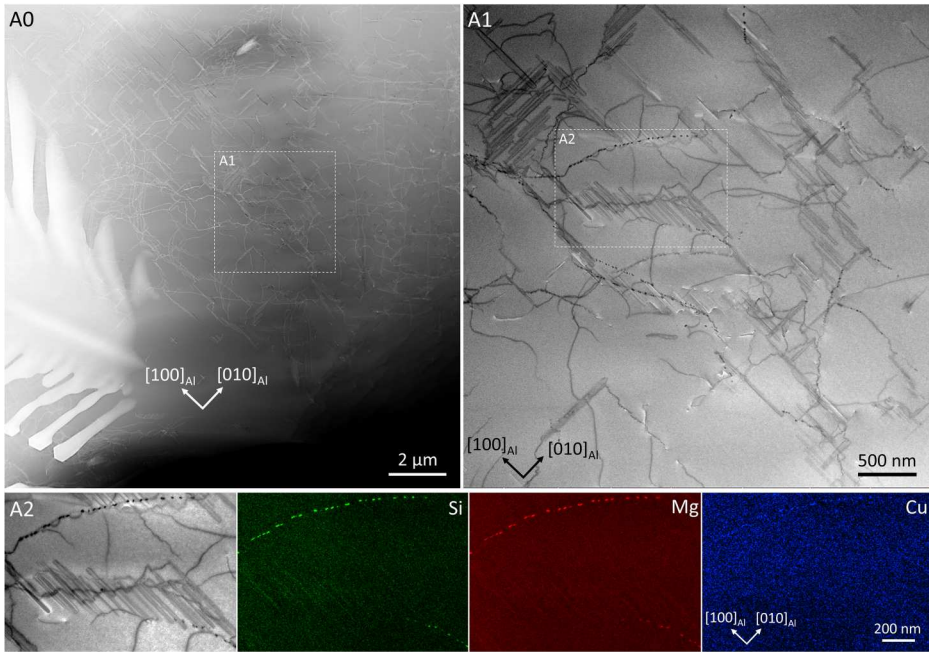
Figure 5. (A0) The HAADF-STEM image of the microstructure along the [001] aluminium zone axis, next to a coarse dendritic feature in the DCGR cast. (A1) The enlarged area marked with dashed white lines in the AO image. (A2) The area marked with white dashed lines in the A1 image and the corresponding elemental maps.

irregular way, and they are not re-arranged into dislocation cell boundaries or polygonised into sub-grain boundaries which indicates that the dislocation network is at its early stage of formation. The origin of dislocation network remains unclear, ranging from the stress concentrations due to segregation, thermal and shrinkage stresses, stresses between the coarse intermetallic particles and Al solid solution, merge of Al dendritic arms with different crystallographic orientation and extremely high solidification rates at the very end of complete solidification [54].

The precipitate nucleation and growth has taken place along the dislocation lines. The precipitates are aligned along the three equivalent $\langle 100 \rangle_{Al}$ directions. The precipitate cross-sections, which are the precipitates whose length is aligned parallel to the incident beam direction, follow closely the dislocation lines. The precipitates tend to align parallel to each other in militaristic formations groups along certain $\langle 100 \rangle_{Al}$ matrix directions. After the nucleation of precipitates has taken place in the dislocation core, their initial direction of growth will be guided by the strain field of the dislocation line. The precipitates nucleating on the dislocation lines with the same Burgers vector will tend to initially grow towards that particular $\langle 100 \rangle_{Al}$ direction, which accommodates the precipitate strain field easier, compared to the two other relative $\langle 100 \rangle_{Al}$ directions. The Figure 5 (A2) shows the elemental maps of precipitate cross-

sections along the dislocation lines. It clearly shows the precipitates nucleated on dislocations are enriched in Si, Mg and Cu, meanwhile the fine precipitates nucleated homogeneously inside Al matrix do not show any Cu presence. The precipitates can form only when their building solute elements, that is Si and Mg are present in the Al matrix within μm range. The required supersaturation of Si and Mg is provided only along the minor segregation bands. It becomes obvious that the precipitate formation has occurred within the segregation bands observed in the EPMA maps (Figure 3).

Figure 6 (A0) shows TEM and STEM images of the microstructure next to a coarse particle in another minor-segregated band in the DCGR cast. The Figure 6 (A1) shows a higher magnification TEM image from the region marked with dashed black lines in the Figure 6 (A0). The dislocation line entanglements cannot be seen in this image, due to their relaxation at the foil surface. Two distinct sub-microstructures can be obviously observed: The one which contains coarse precipitates nucleated heterogeneously along the dislocation lines which are grown along $\langle 100 \rangle_{Al}$ direction in group alignments and the other one with very fine precipitation distributed homogeneously inside the Al matrix, away from the heterogeneously nucleated precipitates.

Heterogeneous nucleation in the dislocation network: High magnification TEM imaging in the Figure 6 (A1) shows the coarse precipitates of around 1 μm length aligned along the three equivalents $\langle 100 \rangle_{Al}$ direction. The precipitates are aligned parallel to each-other along one of the $\langle 100 \rangle_{Al}$, encouraged in their initial stage of growth by the strain field of the dislocation lines. The precipitate-free zones are formed next to the coarse precipitates, due to the matrix depletion of solute and vacancies, which have sunk into the dislocation core lines. The Figure 6 (A2) shows high magnification HAADF-STEM image from the area marked with dashed black lines in the Figure 6 (A1). It reveals the cross-section of precipitates which have favourably nucleated and grown with the aid of dislocation lines. The precipitates are formed in string-like cross-section with significantly big step ledges, as clearly observed particularly in the precipitate 2. The precipitate cross-sections show a mottled intensity distribution, with some parts of the cross-section areas yielding brighter contrast due to enrichment from Cu atoms (Figure 6 (1 & 2)). The atomic-scale imaging of the precipitate cross-sections is carried out in the areas marked with white dashed lines in the precipitate 1 & 2. The precipitates are formed by the triangular arrangement of atoms which patterns help for phase identification. The precipitate cross-section interface is confined and have transversely grown along the $\langle 510 \rangle_{Al}$ direction. The overlayed colour mapping of atomic columns shows the green-coloured positions corresponding to the Si-rich atomic columns and the blue-coloured position corresponding to the Cu-rich atomic column. The Si atomic columns are distributed throughout the precipitate cross-section meanwhile the Cu-rich atomic columns are distributed discretely in blotchy arrangements due to low Cu concentration. The Si-rich
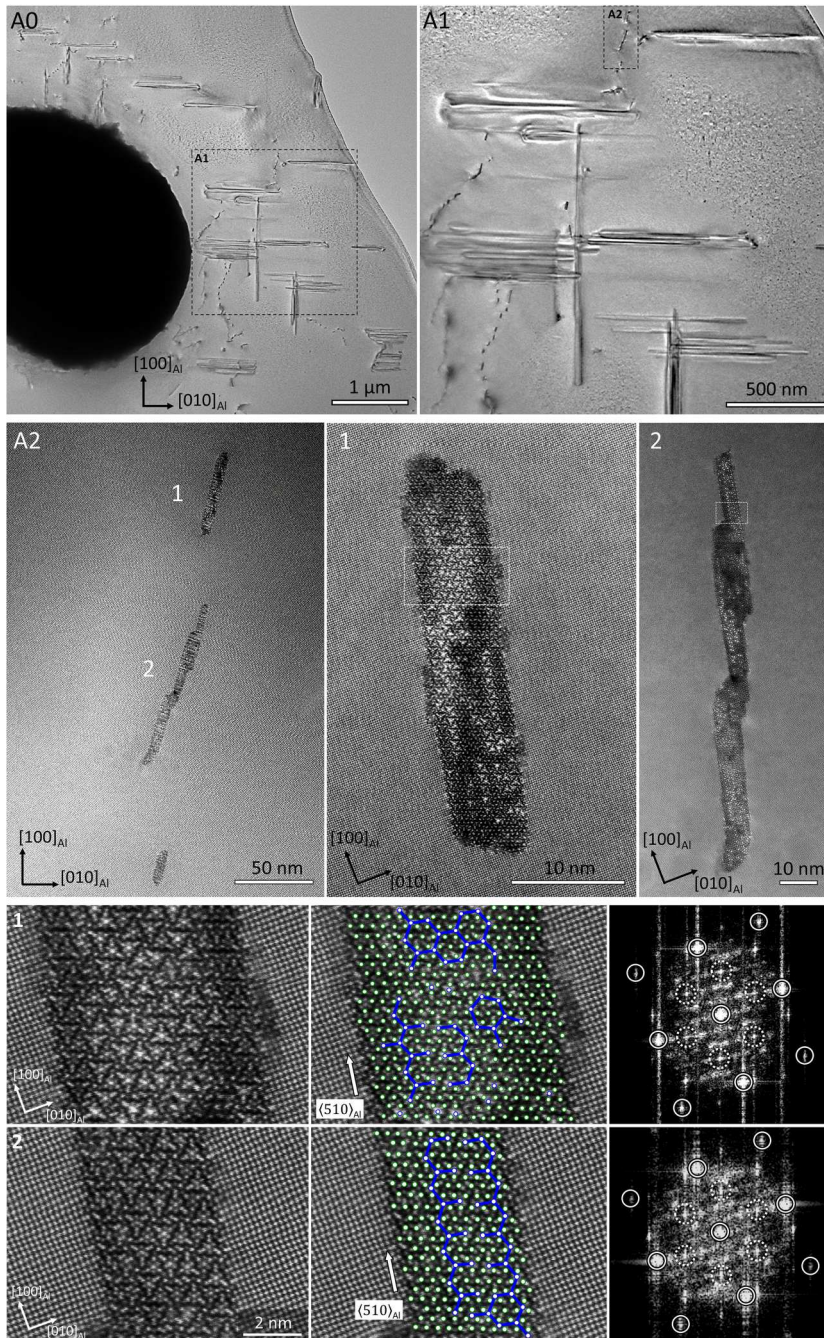
Figure 6. The TEM and STEM imaging along the [001] aluminium zone axis, next to a coarse intermetallic in the minor-segregation bands in the DCGR cast. (A0) TEM image of the micro-structure next to a coarse intermetallic. (A1) The enlarged TEM image of the area marked with dashed black lines in the A0 image. (A2) The HAADF-STEM image of the area marked with dashed black lines in the upper part of the A1 image. (1 & 2) The precipitates 1 and 2 imaged in their entirety using HAADF-STEM mode. The unfiltered atomic-scale images of the cross-sections of the precipitates 1 and 2 marked with white dashed lines. The overlaying of the Si-rich atomic columns in green and Cu-rich atomic columns in blue, and the corresponding FFTs. In the FFTs, the white circles indicate the Al matrix, and the white dashed circles indicate the Si network reflections.

atomic columns form a hexagonal network which is indicated by the dashed circles in the corresponding Fast Fourier Transformations (FFT) [55]. The Si-hexagonal network has been reported as the backbone upon which precipitate forming atoms organise to form a range of phases [55].

To have a complete understanding of the microstructure and phases present along the minor-segregated bands, atomic-scale observation using HAADF-STEM was carried out in the cross-sections of the heterogeneous precipitates. Figure 7 shows the atomic-scale observation from two different precipitates. The precipitates are composed from a mixture of different phases. Figure 7(a, b) shows a part of the precipitate cross-section where the Type-B/U2, β′-Cu, Q′, Type-C/B′ and sub-unit cells of the β′ phases are identified. The high-intensity columns are due to the Cu atoms enrichment. The Cu atoms are present in
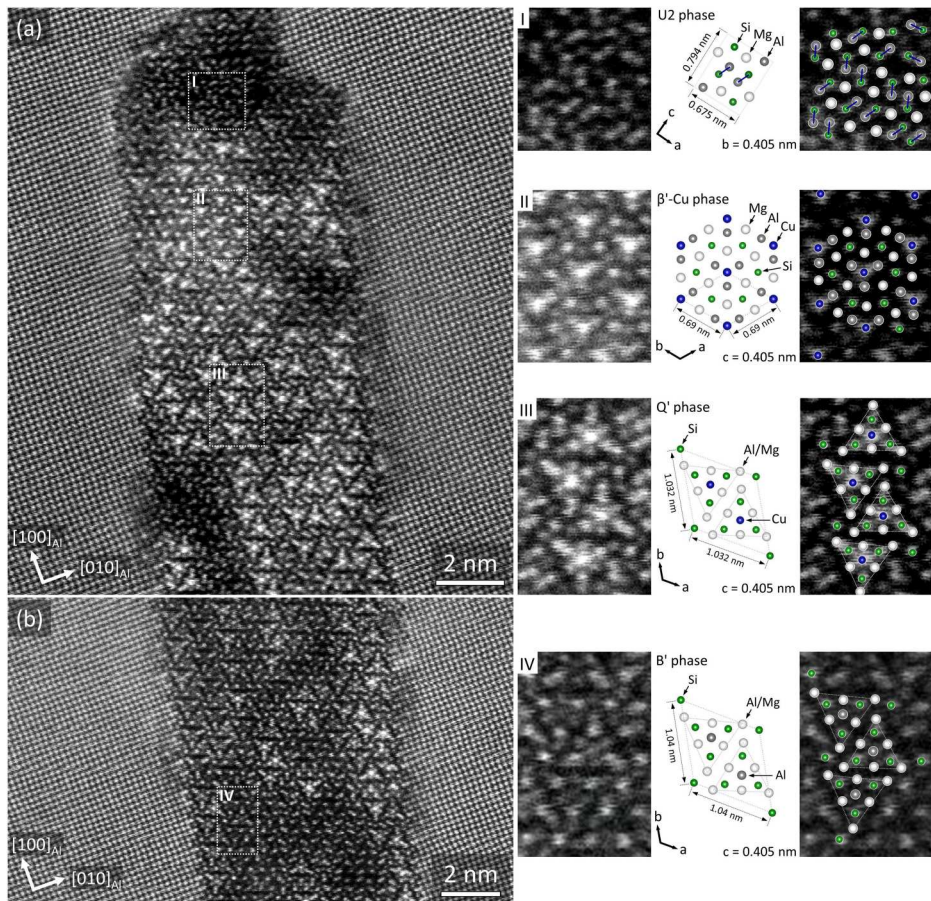
Figure 7. (a, b) The unfiltered atomic-scale HAADF-STEM images along the [001] aluminium zone axis, revealing the precipitate cross-sections of the heterogeneously nucleated precipitates. (I, II, III, IV) The enlarged parts from the different precipitate cross-section areas and the respective metastable phases. The atomic coordinates of the atomic columns parallel with the incident beam (z-coordinates) are neglected.

the formation of the β′-Cu and Q′ phases. Lack of Cu causes replacement from Al atoms which leads to the formation of the B′ phase [56]. All identified phases have the unit cell dimension parallel to the incident beam direction equal to 0.405 nm which equals the interplanar spacing of the (001) Al matrix atomic planes. The equal unit cell dimension perpendicular to the screen, serves to connect all the phases, binding them together in one coarse precipitate and at the same time serves to maintain coherency with the Al matrix. The mixture of phases observed in this image does not represent all heterogeneous precipitates along the minor micro-segregated bands. The variation in the Mg/Si ratio and Cu content across the minor-segregation bands will influence the mixture of phases.

The precipitation depends on the microstructural defects, temperature, exposure length to temperature, cooling rate and the chemical composition of alloy. The dislocations in this regard are not commonly desired defects, as they serve as sinks for solutes and vacancies from the surrounding matrix. The vacancies are well-known to control the precipitation process via solute trapping and diffusion inside the matrix [57–59]. The heterogeneous nucleation of precipitates in dislocation lines is observed commonly in the downstream thermo-mechanical treatment. For example, nucleation on the dislocation lines which had recovered into dislocation cell boundaries or low-angle sub-grain boundaries, had been observed in samples after homogenisation heat treatment [60,61]. The precipitates after homogenisation heat treatment were composed of (Type-B/U2 & Type-C/B′) or (Type-B/U2 & Type-A/U1) for high cooling rate (~830°C/hour), and mainly Type-A/U1 for low cooling rate of (~20°C/hour) in excess-Si alloys [60] and a mixture of (β′ & Type-B/U2) regardless of the cooling rate in the balanced alloys [61]. The heterogeneous nucleation, during artificial ageing, in the dislocation network formed from pre-deformation, was observed in several reports. In the samples with Cu content, the heterogeneously nucleated precipitates were made of a mixture of Q′ phase, β′-Cu phase, C phase, C-1 phase which is isostructural with the C-phase but with another orientation relationship with Al matrix and the L-phase which is the disordered version of the C-phase [62,63]. Other reports show the heterogeneous nucleation was composed of a mixture of Type-C/B′, Type-B/U2, β′ phase and another proposed version of B′, named B′-2 [64]. Depending on composition, heterogeneous precipitates of Type-C/B′ were observed in the excess Si alloys and β′ phase in the balanced alloys [65]. The microstructure of heavily deformed and aged Al-Mg-Si-Cu alloys was composed of heterogeneous precipitates consisting of a mixture of C-phase, E-phase and disordered phases meanwhile the homogenous precipitates in the bulk consisted of L-phases [66]. In case of increased Cu content, the S′ phase would appear in the mixed structure of C, E and disordered phase meanwhile the GBP zones would appear homogenously in the bulk in addition to the L-phase [67].

The Type-A, Type-B and Type-C phases are labelled as U1, U2 and B′, respectively [68–73]. The Type-C or B′ which precipitates in Al-Mg-Si alloys with excess-Si, has the same atomic arrangements as the metastable Q′ crystal structure which precipitates in Al-Mg-Si alloys with Cu addition [65,74–76]. The metastable Q′ phase has its interface extended parallel to the $\langle 510 \rangle_{Al}$ direction, which indicates perseverance of coherency with Al matrix [77,78]. The Q′ has the same crystal structure as the Q phase, but with slightly different unit cell dimensions to better fit to the surrounding Al matrix [79,80]. This is not the case with the stable Q phase which creates multiple orientation relationships with Al matrix due to loss of coherency [81]. The lath-shaped morphologies with cross-section elongated along the $\langle 510 \rangle_{Al}$ direction are classified as the Q′ phase, the plate-shaped ones with cross-section elongated along the $\langle 100 \rangle_{Al}$ are classified as the C-phase in case its structure is ordered or as L-phase in case it is disordered [82]. The degree of ordering is clearly observed in the FFTs, in which the presence of sharp and clear FFT spots indicates ordering while the diffuse and non-symmetrically scattered FFT spots indicate disorder [82].

Homogeneous nucleation inside the aluminium matrix: The very fine precipitates are observed in the areas away from the precipitation free zones. The TEM image in Figure 8 (A0) shows the same image as in the Figure 6. It is seen that very fine precipitates are distributed homogeneously throughout the Al matrix. To gain better understanding of this region, atomic scale imaging was carried out in the area marked with the dashed black lines in Figure 8 (A0). Figure 8 (A1) shows that the precipitates are aligned along the three equivalents $\langle 100 \rangle_{Al}$ matrix direction. The precipitates longitudinal dimension of the heterogeneously nucleated on the dislocation lines are approximately 20 times bigger than that of homogeneously nucleated inside the dislocation-free Al matrix. That is around 390 nm ± 60 nm for the heterogeneous nucleation compared to 20 nm ± 5 nm for the homogeneous ones. The atomic-scale imaging of the precipitate cross-sections and the corresponding FFTs, indicate that they are mainly precursors of the β″ and Type-B/U2 phases (Figure 8(a,b)). The homogeneously nucleated precipitates will develop slowly compared to the fast-track solute-diffusion dislocation-core enhanced. This will cause delaying in phase development and will lead to phases of earlier stages in the precipitation sequence inside the Al matrix compared to the later stages along the dislocation line defects.

The solid-state segregation phenomenon is well investigated in the as-cast condition and in the down-stream thermo-mechanical treatment as well [9,83–85]. The atomic resolved microstructures of the segregation bands are not reported in the as-cast conditions. The precipitates of earlier stage of nucleation had been observed in the matrix, which were the precursor of the β″ phase [63,65,86]. The presence of precipitates heterogeneously grown in the dislocation network and homogeneously inside the Al matrix, were
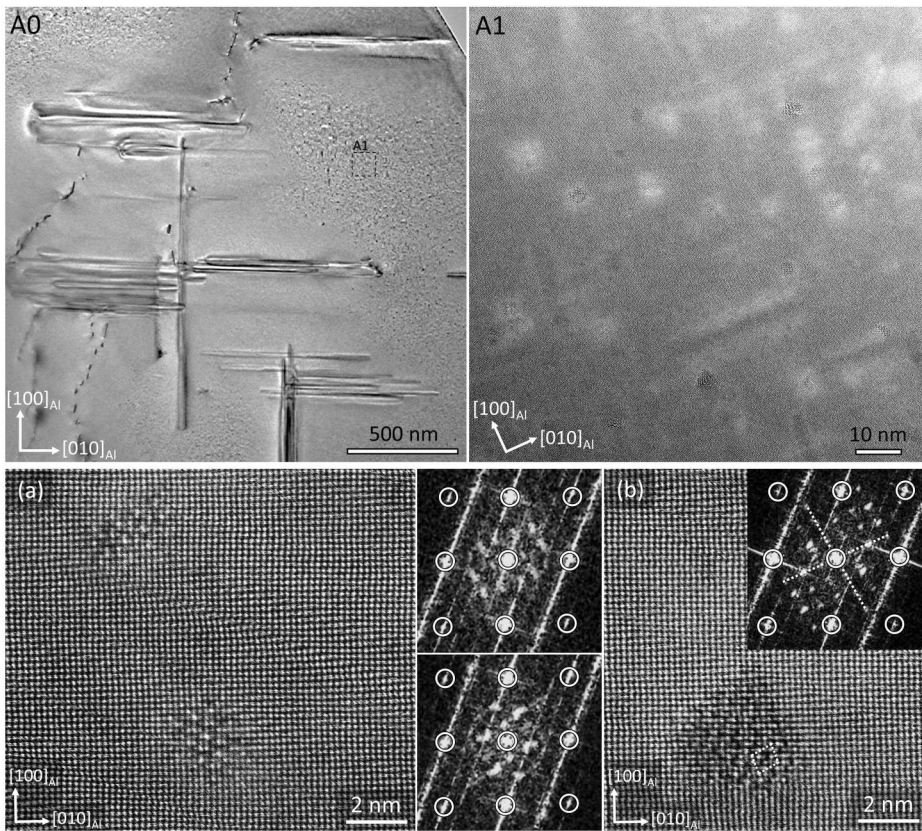
Figure 8. The TEM and STEM image of the microstructure in the minor-segregation bands in the DCGR cast. (A0) The TEM image of the same area as in the Figure 6 (A1). (A1) The enlarged HAADF-STEM image of the area marked with dashed black lines in the A0 image. The homogenous precipitation has taken place. (a, b) The unfiltered atomic-scale HAADF-STEM image of the precipitates homogeneously nucleated inside the Al matrix and their corresponding FFTs.

confirmed along the minor micro-segregated bands in the DC and DCMC cast samples as well (see appendix).

Figure 9 shows the EPMA maps of the DCGR cast as previously shown in Figure 3. The maps are selected considering that the grain boundary and the inter-dendritic channels are clearly observed. The Fe segregation maps are shown in the appendix; however, the Mn segregation map is a good representation of Fe segregation map since it overlaps almost perfectly with it. The network of the minor micro-segregation bands which are composed primarily of Si and Mg segregation are shown in the light grey colour. The minor segregation bands follow the grain boundaries and branch towards the interior of the grain guided by the inter-dendritic channels. The high concentration of Si, Mg, Fe & Mn are shown with the dark grey colour. The intense and continuous segregation of them has clearly occurred along the grain boundaries. However, the discrete and localised regions of high concentrations are seen diverging
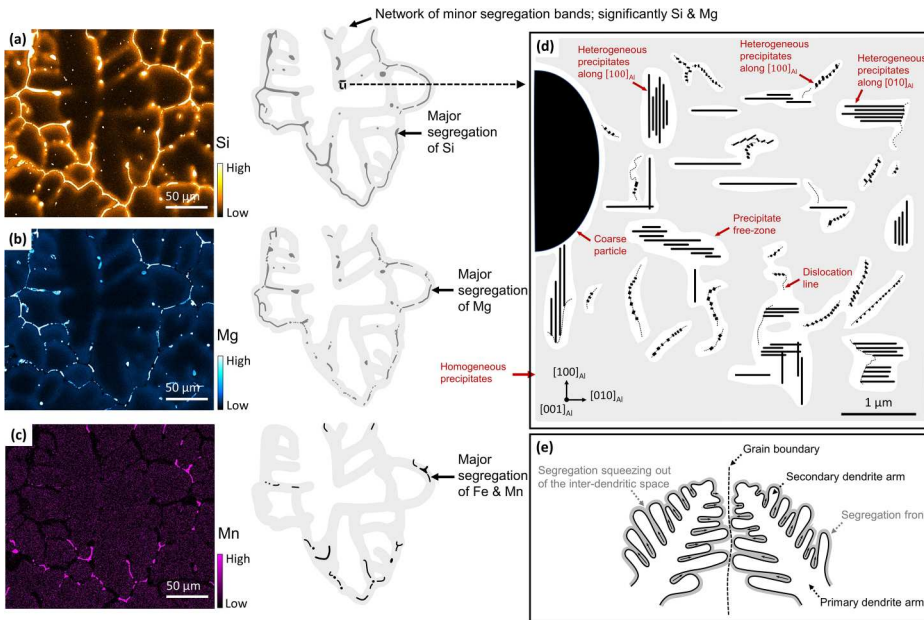
Figure 9. The EPMA maps of segregation pattern in the DCGR cast. (a) The Si segregation map and its schematic. (b) The Mg segregation map and its schematic. (c) The Mn segregation map and its schematic. The Mn segregation map is equivalent to the Fe segregation map. Check Appendix. (d) Illustration of the microstructure of the minor-segregation band. (e) Two aluminium dendrites prior to the bump into an aluminium dendritic boundary.

occasionally towards the grain interior, or deep inside the grains, following inter-dendritic channels.

The network of minor segregation band is the pathway where the precipitates had either nucleated heterogeneously in the dislocation lines, aligning in militaristic group arrangements, or homogenously inside the Al matrix as illustrated in the Figure 9(d). The Si and Mg atoms distributed in the minor-segregation bands have taken part in precipitate formation going out of the Al matrix solid solution. The minor segregation bands contain fine Fe-rich intermetallic, Si-rich dendrites and other phases which are related to the discretely localised high-concentration of elements. The coarse and fine Fe-rich intermetallic and other phases are contained within the network of the minor segregation bands which is a mixture of heterogeneous and homogenous precipitation.

The pattern of segregation occurs because of the squeeze-out occurring at the last stage of solidification as illustrated in the Figure 9(e). The Al dendrites solidification front progress with the continuous build-up of segregation solute in front of it, which is continuously confined by the space between the Al dendritic arms. The continuous confinement of space between the Al dendrites will squeeze out the segregation and force it into the grain boundary, as it is shown with the black arrows in Figure 9(e). This moment will coincide with

the bump of Al dendrites into a grain boundary which will create a segregation pattern as shown in the illustration of the EPMA maps. During the squeeze out, often pocket of high concentration will be trapped deep inside the inter-dendritic channel followed by a path of minor segregation directed towards grain boundary. The grain boundary itself will be significantly enriched due to the overlap of the segregation fields fronts and due to the squeeze out from the inter-dendritic channels. The dislocation network coupled with the segregated elements provides the supersaturation conditions for precipitation formation along the inter-dendritic channels.

Conclusions

Investigation of the micro-segregation patterns in the as-cast AA6082 aluminium alloys lead to the following conclusions:

(1) The micro-segregation patterns of direct chill cast, direct chill cast with grain refiners and direct chill cast with melt conditioning were investigated using spectroscopy and electron microscopy. Due to variations in the patterns of micro-segregation and relatively small sampling volumes, the differences between the three casts were not able to be converted into statistically meaningful ones.

(2) The micro-segregation pattern under all three casting conditions can be divided into major micro-segregation and minor micro-segregation. The major segregation bands consist mainly of Fe, Mn and Si whereas the minor segregation bands consist of Si and Mg. All major segregation bands are flanked by minor segregation bands whereas the minor segregation bands may be present alone.

(3) The alpha-phase $Al_{15}(FeMn)_3Si_2$ is the main intermetallic compound in the major segregation bands and is mainly distributed along the grain boundaries due to the squeeze out of solute-enriched fields from the inter-dendritic channels towards the grain boundaries. The squeeze-out is also responsible for the divergent segregation from the grain boundary towards the grain interior. However, localised, and discrete pockets of abruptly major segregation are also present deep inside the Al grains due to trap from lateral coalescence of the Al dendritic arms.

(4) The minor segregation bands follow the inter-dendritic channels between the Al dendritic arms and grain boundaries. The typical width of the minor segregation bands is 5–15 μm with Mg and Si concentrations peaking at around 0.6–0.8 at.%. The Mg/Si ratio varies across the minor segregation bands.

(5) The irregular dislocation network, at its early stages of development, is heterogeneously distributed across different grains. The heterogeneous precipitation occurs when there is an overlap of the dislocation network

with the supersaturated Al matrix. The precipitation is heterogeneous in the irregular dislocation networks, or homogeneous inside the dislocation-free Al matrix. The precipitates nucleated heterogeneously in the dislocation network are coarser with approximately 20 times the longitudinal size of the homogeneous precipitates, due to the favourable fast-track solute diffusion paths provided by the dislocation core lines.

(6) The heterogeneously formed precipitates are composed of a mixture of phases, such as Type-B/U2, β′-Cu, Q′, Type-C/B′ phases and sub-unit cells of the β′, whereas the homogenously formed precipitates are mono-phases of β″, precursors of the β″ and Type-B/U2 phases. The dislocation networks accelerate the development of the heterogeneously nucleated phases further down the precipitation sequence compared to the phases embedded in the dislocation-free Al matrix. The phase types and local population density of the precipitates depend on the local supersaturation of Si, Mg and Cu which varies across different minor-segregation bands; therefore, the distribution of the precipitate phases is significantly variable.

(7) The two main precipitate-forming solute elements, Si and Mg, were readily observed in the minor-segregation bands, however Cu due to its low concentration was only observed in blotchy patterns on the cross-section of the heterogeneously nucleated precipitates.

(8) The minor-segregation bands form an interconnected network, which follows the inter-dendritic channels between the Al dendritic arms and grain boundaries. Both coarse and fine intermetallic phases are confined within the network of the minor segregation bands, in which the solute supersaturation has nucleated heterogeneous and homogeneous precipitates.

Disclosure statement

Funding

References

[1] D.G. Eskin, R. Nadella, and L. Katgerman, *Effect of different grain structures on center-line macrosegregation during direct-chill casting*. Acta Mater. 56 (2008), pp. 1358–1365. doi:10.1016/j.actamat.2007.11.021.

[2] Z. Yao, Y. Huo, M. Li, and J. Allison, *A quantitative study of microsegregation in aluminum–copper alloys*. Metall. Mater. Trans. A 53 (2022), pp. 2383–2401. doi:10.1007/s11661-022-06669-3.

[3] R. Nadella, D.G. Eskin, Q. Du, and L. Katgerman, *Macrosegregation in direct-chill casting of aluminium alloys*. Prog. Mater. Sci. 53 (2008), pp. 421–480. doi:10.1016/j. pmatsci.2007.10.001.

[4] X. Doré, H. Combeau, and M. Rappaz, *Modelling of microsegregation in ternary alloys: applications to the solidification of Al-Mg-Si*. Acta Mater. 48 (2000), pp. 3951–3962. doi:10.1016/S1359-6454(00)00177-4.

[5] Q. Dong, X. Chen, J. Xia, X. Li, B. Zhang, and H. Nagaumi, *Floating grain characterization and its effects on centerline segregation of direct-chill cast Al-Mg-Si alloy billets*. Mater. Trans. 61(12) (2020), pp. 2386–2392. doi:10.2320/matertrans.MT-M2020229.

[6] L. Lodgaard and N. Ryum, *Precipitation of dispersoids containing Mn and/or Cr in Al–Mg–Si alloys*. Mater. Sci. Eng. 283 (2000), pp. 144–152. doi:10.1016/S0921-5093 (00)00734-6.

[7] R. Hu, T. Ogura, H. Tezuka, T. Sato, and Q. Liu, *Dispersoid formation and recrystallization behavior in an Al-Mg-Si-Mn alloy*. J. Mater. Sci. Technol. 26(3) (2010), pp. 237–243. doi:10.1016/S1005-0302(10)60040-0.

[8] M. Kenyon, J. Robson, J. Fellowes, and Z. Liang, *Effect of dispersoids on the microstructure evolution in Al–Mg–Si alloys*. Adv. Eng. Mater. 21 (2019), pp. 1800494. doi:10. 1002/adem.201800494.

[9] T. Dorin, M. Ramajayam, S. Babaniaris, and T.J. Langan, *Micro-segregation and precipitates in as-solidified Al-Sc-Zr-(Mg)-(Si)-(Cu) alloys*. Mater. Charact. 154 (2019), pp. 353–362. doi:10.1016/j.matchar.2019.06.021.

[10] Y.S. Park, S.B. Lee, and N.J. Kim, *Microstructure and mechanical properties of strip cast Al-Mg-Si-X alloys*. Mater. Trans. 44(12) (2003), pp. 2617–2624. doi:10.2320/ matertrans.44.2617.

[11] M. Ganesan, L. Thuinet, D. Dye, and P.D. Lee, *Quantification of microsegregation in cast Al-Si-Cu alloys*. Metall. Mater. Trans. 38 (2007), pp. 557–566. doi:10.1007/ s11663-007-9071-0.

[12] G. Scamans, *Electric vehicle spike demand for high strength aluminum extrusions*. Light Met. Age 76 (2018), pp. 6-12.

[13] C.D. Marioara, S.J. Andersen, J. Jansen, and H.W. Zandbergen, *The influence of temperature and storage time at RT on nucleation of the β'' phase in a 6082 Al-Mg-Si alloy*. Acta Mater. 51 (2003), pp. 789–796. doi:10.1016/S1359-6454(02)00470-6.

[14] A. Cibula, *The grain refinement of aluminium alloy castings by additions of titatnium and boron*. J. Inst. Met. 80 (1951), pp. 1–16.

[15] Z. Fan, Y. Wang, Y. Zhang, T. Qin, X.R. Zhou, G.E. Thompson, T. Pennycook, and T. Hashimoto, *Grain refining mechanism in the Al/Al-Ti-B system*. Acta Mater. 84 (2015), pp. 292–304. doi:10.1016/j.actamat.2014.10.055.

[16] Z. Fan, *An epitaxial model for heterogenous nucleation on potent substrates*. Metall. Mater. Trans. A 44 (2013), pp. 1409–1418. doi:10.1007/s11661-012-1495-8.

[17] Z. Fan, B. Jiang, and Y. Zuo. *Apparatus and method for liquid metals treatment*. WO/ 2012/035357 and 2013 US 20130228045 A1.

[18] G. Scamans, H.T. Li, J.L. Nebreda, J. Patel, I. Stone, Y. Wang, X. Yang, and Z. Fan, *Advanced casting technologies using high shear melt conditioning*. Fundam. Alum. Metall., Chapter 8 (2018), pp. 249–277. doi:10.1016/B978-0-08-102063-0.00008-4.

[19] J.B. Patel, H.T. Li, X. Mingxu, and S. Jones, *Melt conditioned direct chill casting (MC-DC) process for production of high-quality aluminum alloy billets*. Mater. Sci. Forum 794-796 (2014), pp. 149–154. doi:10.4028/www.scientific.net/MSF.794-796.149.

[20] K.M.S. Manu, N.S. Barekar, J.L. Nebreda, J.B. Patel, and Z. Fan, *In-situ microstructural control of A6082 alloy to modify second phase particles by melt conditioned direct chill*

(MC-DC) casting process – a novel approach. J. Mater. Process. Technol. 295 (2021), pp. 117170. doi:10.1016/j.jmatprotec.2021.117170.

[21] G. Scamans, H.T. Li, and Z. Fan, *Melt conditioned casting of aluminum alloys*, 13th International Conference on Aluminum Alloys (ICAA13), 2012. doi:10.1007/978-3-319-48761-8_213.

[22] S. Kumar and K.A.Q. O'Reilly, *Influence of Al grain structure on Fe bearing intermetallics during DC casting of an Al-Mg-Si alloy*. Mater. Charact. 120 (2016), pp. 311–322. doi:10.1016/j.matchar.2016.09.017.

[23] S. Kumar, P.S. Grant, and K.A.Q. O'Reilly, *Evolution of Fe bearing intermetallics during DC casting and homogenization of an Al-Mg-Si Al alloy*. Metall. Mater. Trans. A 47 (2016), pp. 3000–3014. doi:10.1007/s11661-016-3451-5.

[24] S. Kumar, P.S. Grant, and K.A.Q. O'Reilly, *Fe bearing intermetallic phase formation in a wrought Al-Mg-Si alloy*. Trans. Indian Inst. Met. 65(6) (2012), pp. 553–557. doi:10.1007/s12666-012-0221-y.

[25] A. Verma, S. Kumar, P.S. Grant, and K.A.Q. O'Reilly, *Influence of cooling rate on the Fe intermetallic formation in an AA6063 Al alloy*. J. Alloys Compd. 555 (2013), pp. 274–282. doi:10.1016/j.jallcom.2012.12.077.

[26] T. Hashimoto, G.E. Thompson, M. Curioni, X. Zhou, and P. Skeldon, *Three-dimensional imaging of light metals using serial block face scanning electron microscopy (SBFSEM)*. Mat. Sci. Forum 765 (2013), pp. 501–505. doi:10.4028/www.scientific.net/MSF.765.501.

[27] J.M. Yu, T. Hashimoto, H.T. Li, N. Wanderka, Z. Zhang, C. Cai, X.L. Zhong, J. Qin, Q.P. Dong, H. Nagaumi, and X.N. Wang, *Formation of intermetallic phases in unrefined and refined AA6082 Al alloys investigated by using SEM-based ultramicrotomy tomography*. J. Mater. Sci. Technol. 120 (2022), pp. 118–128. doi:10.1016/j.jmst.2022.02.007.

[28] C.M. Dinnis, J.A. Taylor, and A.K. Dahle, *As-cast morphology of iron-intermetallics in Al-Si foundry alloys*. Scr. Mater. 53 (2005), pp. 955–958. doi:10.1016/j.scriptamat.2005.06.028.

[29] Z. Que and C.L. Mendis, *Heterogenous nucleation and phase transformation of Fe-rich intermetallic compounds in Al-Mg-Si alloys*. J. Alloys Compd. 836 (2020), pp. 155515. doi:10.1016/j.jallcom.2020.155515.

[30] Z. Que, Y. Wang, and Z. Fan, *Formation of the Fe-containing intermetallic compounds during solidification of Al-5Mg-2Si-0.7Mn-1.1Fe alloy*. Metall. Mater. Trans. A 49 (2018), pp. 2173–2181. doi:10.1007/s11661-018-4591-6.

[31] Y.L. Liu and S.B. Kang, *The solidification process of Al–Mg–Si alloys*. J. Mater. Sci. 32 (1997), pp. 1443–1447. doi:10.1023/A:1018545732009.

[32] Y.L. Liu, S.B. Kang, and H.W. Kim, *The complex microstructures in an as-cast Al–Mg–Si alloy*. Mater. Lett. 41 (1999), pp. 267–272. doi:10.1016/S0167-577X(99)00141-X.

[33] Z. Fan, M. Xia, H. Zhang, G. Liu, J.B. Patel, Z. Bian, I. Bayandorian, Y. Wang, H.T. Li, and G.M. Scamans, *Melt conditioning by advanced shear technology (MCAST) for refining solidification microstructure*. Int. J. Cast Met. Res. 22(1-4) (2009), pp. 103–107. doi:10.1179/136404609X367443.

[34] Z. Fan, Y. Wang, Z.F. Zhang, M. Xia, H.T. Li, J. Xu, L. Granas, and G.M. Scamans, *Shear enhanced heterogenous nucleation in some Mg-and Al-alloys*. Int. J. Cast Met. Res. 22(1-4) (2009), pp. 318–322. doi:10.1179/136404609X367452.

[35] D. Luo, I. Chang, J.B. Patel, K. Al-Helal, Y. Huang, G.M. Scamans, and Z. Fan, *Microstructure and mechanical properties of recycled AA6111 alloy processed by melt conditioned direct chill (MC-DC) casting*. M&Ns-19 (17-19 July 2019), pp. 81–85.

[36] S.H. Oh, Y. Kauffmann, C. Scheu, W.D. Kaplan, and M. Rühle, *Ordered liquid aluminum at the interface with sapphire*. Science 310(5748) (2005), pp. 661–663. doi:10.1126/science.1118611.

[37] H.T. Li, Y. Wang, and Z. Fan, *Enhanced heterogeneous nucleation on oxides in Al alloys by intensive shearing*. IOP Conf. Ser.: Mater. Sci. Eng. 27 (2012), pp. 012047. doi:10.1088/1757-899X/27/1/012047.

[38] J.L. Nebreda, J.B. Patel, I. Stone, and G.M. Scamans, *De-ironing of aluminium alloy scrap by high shear melt conditioning technology*, Proceedings of the 6th Decennial International Conference on Solidification Processing, Old Windsor, July 2017. doi:10.3390/met12101579.

[39] Z.P. Que, Y.P. Zhou, Y. Wang, and Z. Fan, *Effect of MgO on phase selection in Al–Mg–Si–Fe–Mn alloys*. Trans. Indian Inst. Met. 68(6) (2015), pp. 1167–1172. doi:10.1007/s12666-015-0664-z.

[40] H.T. Li, S. Ji, Y. Wang, M. Xia, and Z. Fan, *Effect of intensive melt shearing on the formation of Fe-containing intermetallics in LM24 Al-alloy*. IOP Conf. Ser.: Mater. Sci. Eng. 27 (2012), pp. 012075. doi:10.1088/1757-899X/27/1/012075.

[41] H.T. Li, M. Xia, P. Jarry, G.M. Scamans, and Z. Fan, *Grain refinement in a AlZnMgCuTi alloy by intensive melt shearing: A multi-step nucleation mechanism*. J. Cryst. Growth 314 (2011), pp. 285–292. doi:10.1016/j.jcrysgro.2010.10.168.

[42] M. Cooper, *The crystal structure of the ternary alloy α(AlFeSi)*. Acta Cryst. 23 (1967), pp. 1106–1107. doi:10.1107/S0365110X67004372.

[43] K. Matsuda, T. Kawabata, Y. Uetani, T. Sato, and S. Ikeno, *Hexagonal tabular β-phase in Al-Mg-Si-Cu alloy*. Scr. Mater. 47 (2002), pp. 467–471. doi:10.1016/S1359-6462(02)00173-2.

[44] C. Li, Y.Y. Wu, H. Li, and X.F. Liu, *Morphological evolution and growth mechanism of primary Mg_2Si phase in Al-Mg_2Si alloys*. Acta Mater. 59 (2011), pp. 1058–1067. doi:10.1016/j.actamat.2010.10.036.

[45] E. Cinkilic, M. Moodispaw, J. Zhang, J. Miao, and A.A. Luo, *A new recycled Al-Si-Mg alloy for sustainable structural die casting applications*. Metall. Mater. Trans. A 53 (2022), pp. 2861–2873. doi:10.1007/s11661-022-06711-4.

[46] C.J. Simensen, P. Fartum, and A. Andersen, *Analysis of intermetallic particles in aluminium by dissolution of the sample in butanol*. Fresenius Z. Anal. Chem. 319 (1984), pp. 286–292. doi:10.1007/BF00487273.

[47] J. Gjønnes, V. Hansen, S.J. Andersen, C.D. Marioara, and X.Z. Li, *Electron crystallography of aluminum alloy phases*. Z. Kristallogr. 218 (2003), pp. 293–307. doi:10.1524/zkri.218.4.293.20745.

[48] N.C.W. Kuijpers, F.J. Vermolen, C. Vuik, P.T.G. Koenis, K.E. Nilsen, and S. van der Zwaag, *The dependence of the β-AlFeSi to α-Al(FeMn)Si transformation kinetics in Al-Mg-Si alloys on the alloying elements*. Mat. Sci. Eng. A 394 (2005), pp. 9–19. doi:10.1016/j.msea.2004.09.073.

[49] K. Al-Helal, J.L. Nebreda, J.B. Patel, and G.M. Scamans, *High-shear de-gassing and de-ironing of an aluminum casting alloy made directly from aluminum end-of-life vehicle scrap*. Recycling 6 (2021), pp. 66. doi:10.3390/recycling6040066.

[50] N.C.W. Kuijpers, W.H. Kool, P.T.G. Koenis, K.E. Nilsen, I. Todd, and S. van der Zwaag, *Assessment of different techniques for quantification of α-Al(FeMn)Si and β-AlFeSi intermetallics in AA6xxx alloys*. Mater. Charact. 49 (2002), pp. 409–420. doi:10.1016/S1044-5803(03)00036-6.

[51] N.C.W. Kuijpers, F.J. Vermolen, K. Vuik, and S. van der Zwaag, *A model of the β-AlFeSi to α-Al(FeMn)Si transformation in Al-Mg-Si alloys*. Mater. Trans. 44(7) (2003), pp. 1448–1456. doi:10.2320/matertrans.44.1448.

[52] H. Tanihata, T. Sugawara, K. Matsuda, and S. Ikeno, *Effect of casting and homogenizing treatment conditions on the formation of Al-Fe-Si intermetallic compounds in 6063 Al-Mg-Si alloys*. J. Mater. Sci. 34 (1999), pp. 1205–1210. doi:10.1023/A:1004504805781.

[53] D.T.L. Alexander and A.L. Greer, *Solid-state intermetallic phase tranformations in 3XXX aluminium alloys*. Acta Mater. 50 (2002), pp. 2571–2583. doi:10.1016/S1359-6454(02)00085-X.

[54] V.S. Zolotorevsky, N.A. Belov, and M.V. Glazoff, *Casting Aluminum Alloys*, Chapter 2, Elsevier Science Ltd., Amsterdam, 2007.

[55] S.J. Andersen, C.D. Marioara, J. Friis, R. Bjørge, Q. Du, I.G. Ringdalen, S. Wenner, E.A. Mørtsell, R. Holmestad, T. Saito, J. Røyset, and O. Reiso, *Directionality and column arrangement principles of precipiatetes in Al-Mg-Si-(Cu) and Al-Mg-Cu linked to line defect in Al*. Mater. Sci. Forum 877 (2016), pp. 461–470. doi:10.4028/www.scientific.net/MSF.877.461.

[56] T. Saito, E.A. Mørtsell, S. Wenner, C.D. Marioara, S.J. Andersen, J. Friis, K. Matsuda, and R. Holmestad, *Atomic structures of precipitates in Al-Mg-Si alloys with small additions of other elements*. Adv. Eng. Mater. 20 (2018), pp. 180015. doi:10.1002/adem.201800125.

[57] S. Pogatscher, H. Antrekowitsch, M. Werinos, F. Moszner, S.S.A. Gerstl, M.F. Francis, W.A. Curtin, J.F. Löffler, and P.J. Uggowitzer, *Diffusion on demand to control precipitation aging: application to Al-Mg-Si alloys*. Phys. Rev. Lett. 112 (2014), pp. 225701. doi:10.1103/PhysRevLett.112.225701.

[58] S. Pogatscher, H. Antrekowitsch, H. Leitner, D. Pöschmann, Z.L. Zhang, and P.J. Uggowitzer, *Influence of interrupted quenching on artificial aging of Al-Mg-Si alloys*. Acta Mater. 60 (2012), pp. 4496–4505. doi:10.1016/j.actamat.2012.04.026.

[59] S. Pogatscher, H. Antrekowitsch, H. Leitner, T. Ebner, and P.J. Uggowitzer, *Mechanisms controlling the artificial aging of Al-Mg-Si alloys*. Acta Mater. 59 (2011), pp. 3352–3363. doi:10.1016/j.actamat.2011.02.010.

[60] S. Qin, A. Bendo, T. Tsuchiya, S. Lee, and K. Matsuda, *Effect of cooling rate on precipitation during homogenization cooling in excess Si type Al-Mg-Si alloy*. Mater. Lett. 278 (2020), pp. 128363. doi:10.1016/j.matlet.2020.128363.

[61] S. Qin, A. Bendo, T. Tsuchiya, S. Lee, Y. Zou, and K. Matsuda, *Effect of cooling rate on precipitation during homogenization cooling in balanced Al-Mg$_2$Si alloy*. Mater. Trans. 61(11) (2020), pp. 2115–2120. doi:10.2320/matertrans.MT-M2020189.

[62] M.R. Gazizov, A.V. Dubina, D.A. Zhemchuzhnikova, and R.O. Kaibyshev, *Effect of equal channel angular pressing and aging on the microstructure and mechanical properties of an Al–Cu–Mg–Si alloy*. Phys. Met. Metallogr. 116(7) (2015), pp. 718–729. doi:10.1134/S0031918X15070066.

[63] M. Gazizov, C.D. Marioara, J. Friis, S. Wenner, R. Holmestad, and R. Kaibyshev, *Precipitation behavior in an Al–Cu–Mg–Si alloy during ageing*. Mater. Sci. Eng. A 767 (2019), pp. 138369. doi:10.1016/j.msea.2019.138369.

[64] Y.X. Lai, W. Fan, M.J. Yin, C.L. Wu, and J.H. Chen, *Structures and formation mechanisms of dislocation-induced precipitates in relation to the age-hardening responses of Al-Mg-Si alloys*. J. Mater. Sci. Technol. 41 (2020), pp. 127–138. doi:10.1016/j.jmst.2019.11.001.

[65] K. Matsuda, S. Shimizu, H. Gamada, Y. Uetani, F. Shinagawa, and S. Ikeno, *Effect of deformation on the precipitates in Al-Mg$_2$Si alloys containing silicon in excess*. Mater. Des. Eng. 48(1) (1999), pp. 10–15. doi:10.2472/jsms.48.10.

[66] E. Thronsen, C.D. Marioara, J.K. Sunde, K. Minakuchi, T. Katsumi, I. Erga, S.J. Andersen, J. Friis, K. Marthinsen, K. Matsuda, and R. Holmestad, *The effect of*

heavy deformation on the precipitation in an Al-1.3Cu-1.0Mg-0.4Si wt.% alloy. Mater. Des. 186 (2020), pp. 108203. doi:10.1016/j.matdes.2019.108203.

[67] E. Thronsen, H. Morkeseth, C.D. Marioara, K. Minakuchi, T. Katsumi, K. Marthinsen, K. Matsuda, and R. Holmestad, *The effect of small additions of Fe and heavy deformation on the precipitation in an Al-1.1Mg-0.5Cu-0.3Si at.% alloy*. Metall. Mater. Trans. 53 (2022), pp. 3296–3310. doi:10.1007/s11661-022-06744-9.

[68] K. Matsuda, S. Tada, S. Ikeno, T. Sato, and A. Kamio, *Crystal system of rod-shaped precipitates in an Al-1.0mass%Mg$_2$Si-0.4mass%Si alloy*. Scr. Metall. Mater. 32(8) (1995), pp. 1175–1180. doi:10.1016/0956-716X(95)00121-B.

[69] K. Matsuda, S. Ikeno, T. Sato, and A. Kamio, *A metastable phase having the orthorhombic crystal lattice in an Al-1.0mass% Mg$_2$Si-0.4mass% Si alloy*. Scr. Mater. 34(11) (1996), pp. 1797–1802. doi:10.1016/1359-6462(96)00057-7.

[70] K. Matsuda, S. Ikeno, T. Sato, and A. Kamio, *Classification of metastable phases in Al-Mg$_2$Si alloys by HRTEM*. Mater. Sci. Forum 217-222 (1996), pp. 707–712. doi:10.4028/www.scientific.net/MSF.217-222.707.

[71] S.J. Andersen, C.D. Marioara, R. Vissers, A. Frøseth, and H.W. Zandbergen, *The structural relation between precipitates in Al-Mg-Si alloys, the Al-matrix and diamond silicon, with emphasis on the trigonal phase U1-MgAl$_2$Si$_2$*. Mater. Sci. Eng. A 444 (2007), pp. 157–169. doi:10.1016/j.msea.2006.08.084.

[72] S.J. Andersen, C.D. Marioara, A. Frøseth, R. Vissers, and H.W. Zandbergen, *Crystal structure of the orthorhombic U2-Al$_4$Mg$_4$Si$_4$ precipitate in the Al–Mg–Si alloy system and its relation to the β' and β" phases*. Mater. Sci. Eng. A 390 (2005), pp. 127–138. doi:10.1016/j.msea.2004.09.019.

[73] S.J. Andersen, C.D. Marioara, A. Frøseth, R. Vissers, and H.W. Zandbergen, *Crystal structures of the trigonal U1-MgAl$_2$Si$_2$ and orthorhombic U2-Mg$_4$Al$_4$Si$_4$ precipitates in the Al-Mg-Si alloy system*. I. Phys. Conf. Ser. 179 (2003), pp. 225.

[74] K. Matsuda, Y. Uetani, T. Sato, and S. Ikeno, *Metastable phases in an Al-Mg-Si alloy containing copper*. Metall. Mater. Trans. A 32 (2001), pp. 1293–1299. doi:10.1007/s11661-001-0219-2.

[75] K. Matsuda, D. Teguri, Y. Uetani, T. Sato, and S. Ikeno, *Cu-seggregation at the Q'/α-Al interface in Al-Mg-Si-Cu alloy*. Scr. Mater. 47 (2002), pp. 833–837. doi:10.1016/S1359-6462(02)00325-1.

[76] S. Wenner, C.D. Marioara, S.J. Andersen, and R. Holmestad, *Effect of room temperature storage time on precipitation in Al-Mg-Si(-Cu) alloys with different Mg/Si ratios*. Int. J. Mater. Res. 103 (2012), pp. 948–954. doi:10.3139/146.110795.

[77] H.S. Hasting, J.C. Walmsley, A.T.J. Van Helvoort, C.D. Marioara, S.J. Andersen, and R. Holmestad, *Z-contrast imaging of the arrangement of Cu in precipitates in 6XXX-series aluminium alloys*. Philos. Mag. Lett. 86(9) (2006), pp. 589–597. doi:10.1080/09500830600938340.

[78] C.D. Marioara, S.J. Andersen, T.N. Stene, H. Hasting, J. Walmsley, A.T.J. Van Helvoort, and R. Holmestad, *The effect of Cu on precipitation in Al-Mg-Si alloys*. Philos. Mag. 87(23) (2007), pp. 3385–3413. doi:10.1080/14786430701287377.

[79] L. Arnberg and B. Aurivillius, *The crystal structure of Al$_X$Cu$_2$Mg$_{12-x}$Si$_7$ (h-AlCuMgSi)*. Acta Chem. Scand. 34a (1980), pp. 1–5.

[80] M. Torsaeter, R. Vissers, C.D. Marioara, S.J. Andersen, and R. Holmestad, *Crystal structure determination of the Q' and C-type plate precipitates in Al-Mg-Si-Cu (6xxx) alloys*, in Jürgen Hirsch, Birgit Skrotzki, Günter Gottstein (Eds.), *Aluminium Alloys: Their Physical and Mechanical Properties*, vol. 2, Wiley-VHC, Aachen, 2008.

[81] M. Fiawoo, X. Gao, L. Bourgeois, N. Parson, X.Q. Zhang, M. Couper, and J.F. Nie, *Formation of multiple orientation relationships of Q precipitates in Al–Mg–Si–Cu alloys.* Scr. Mater. 88 (2014), pp. 53–56. doi:10.1016/j.scriptamat.2014.05.013.

[82] M. Torsaeter, W. Lefebvre, C.D. Marioara, S.J. Andersen, J.C. Walmsley, and R. Holmestad, *Study of intergrown L and Q' precipitates in Al–Mg–Si–Cu alloys.* Scr. Mater. 64 (2011), pp. 817–820. doi:10.1016/j.scriptamat.2011.01.008.

[83] G.M. Scamans, N.J.H. Holroyd, and C.D.S. Tuck, *The role of magnesium segregation in the intergranular stress corrosion cracking of aluminium alloy.* Corros. Sci. 27(4) (1987), pp. 329–347. doi:10.1016/0010-938X(87)90076-X.

[84] X. Sauvage, N. Enikeev, R. Valiev, Y. Nasedkina, and M. Murashkin, *Atomic-scale analysis of the segregation and precipitation mechanisms in a severely deformed Al–Mg alloy.* Acta Mater. 72 (2014), pp. 125–136. doi:10.1016/j.actamat.2014.03.033.

[85] M. de Hass and J.T.M. De Hosson, *Grain boundary segregation and precipitation in aluminium alloys.* Scripta Mater. 44 (2001), pp. 281–286. doi:10.1016/S1359-6462 (00)00577-7.

[86] K. Teichmann, C.D. Marioara, S.J. Andersen, and K. Marthinsen, *The effect of preaging deformation on the precipitation behavior of an Al-Mg-Si alloy.* Metall. Mater. Trans. A 43 (2012), pp. 4006–4014. doi:10.1007/s11661-012-1235-0.